RESEARCH ARTICLE

Characterising the wind-advected medial fall deposit from fissure 8 fountaining during the 2018 lower East Rift Zone eruption, Kīlauea

Emma J. Watts[1] · Wendy A. Cockshell[2] · Bruce F. Houghton[2]

Abstract

The 2018 eruption on the lower East Rift Zone, Hawaii, involved the opening of 24 fissures before the eruption focussed on a single point source, fissure 8 (F8). This study characterises the preserved medial F8 tephra deposit using an isopach map, maximum clast size data, and total grain size distribution analysis, shedding light on the tephra transport and dispersal mechanisms beyond the F8 cone occurring during the fountaining. The medial sheet-like deposit covers approximately 0.22 km^2, best fit by a Power-Law thinning rate. The TephraFits model estimated the corresponding volume of the continuous medial tephra blanket to be $\sim 2 \times 10^4$ m^3, just 0.02% of the total volume erupted from fissure 8. Samples from the preserved medial deposit have grain size modes of -3.5 to -4 Φ, compatible with Voronoi tessellation calculations. Maximum clast size did not show a 'typical' fining relationship with distance from the vent; instead, it shows no clear pattern. One factor was that the extremely low clast density, a function of a secondary vesiculation event, enabled the pyroclasts to be re-entrained, often repeatedly, by large eddies downwind of the vent. This should be considered in future studies of prolonged fountaining episodes as the clasts involved in the medial fall are rarely well preserved in the geologic record due to their fragile nature but their presence adds complexity to the inferred eruption dynamics.

Keywords Tephra deposit · lower East Rift Zone · Hawaiian Fountaining · Grain size · Vesicularity · Reticulite

Introduction

In 2018, an extended period of low (~ 80 m) Hawaiian fountaining occurred within the lower East Rift Zone (LERZ), Hawaii. Activity soon focussed on a single fissure, fissure 8 (F8, Fig. 1), that was situated in the middle of a residential area, known as Leilani Estates. The eruption created a 13-km-long lava flow field (Dietterich et al. 2021) and a new ~ 40-m-high scoria cone, comprised of course-grained tephra, both causing extensive damage to properties and infrastructure (Meredith et al. 2022). Given the sparsity of Hawaiian fountaining studies and the level of risk that Hawaiian fountain eruptions pose to society, understanding the volume, grain size distribution, and eruption dynamics is vital to accurately assess the risk of future eruptions.

Tephra is fragmented material ejected during an explosive eruption and can be further classified in three size ranges: bombs (> 64 mm), lapilli (2–64 mm), and ash (< 2 mm). The tephra of Hawaiian fountaining events commonly contains Pele's hair and other glassy fragments which can cause eye and skin irritation. This along with other hazards associated with these events, such as respiratory issues (Horwell et al. 2008; Longo et al. 2010), a reduction in agricultural productivity, and long-term property and infrastructural damage (Longo 2013), makes field characterisation and modelling of tephra dispersal an important field of research (Wilson et al. 2012; Jenkins et al. 2015, 2018).

Tephra deposits can be characterised by isopach and isopleth maps, vesicularity, and total grain size distribution (TGSD); each shedding light on the dynamics of tephra production and dispersal. In the last decade, statistical toolboxes have been developed to estimate eruption volumes (Biass et al. 2019a, 2019b) and to integrate grain size data obtained in the field to produce a TGSD (Biass and Bonadonna 2014). Based on the errors associated with field measurements and

✉ Emma J. Watts
e.watts@soton.ac.uk

1   School of Ocean and Earth Science, University of Southampton, Southampton, UK

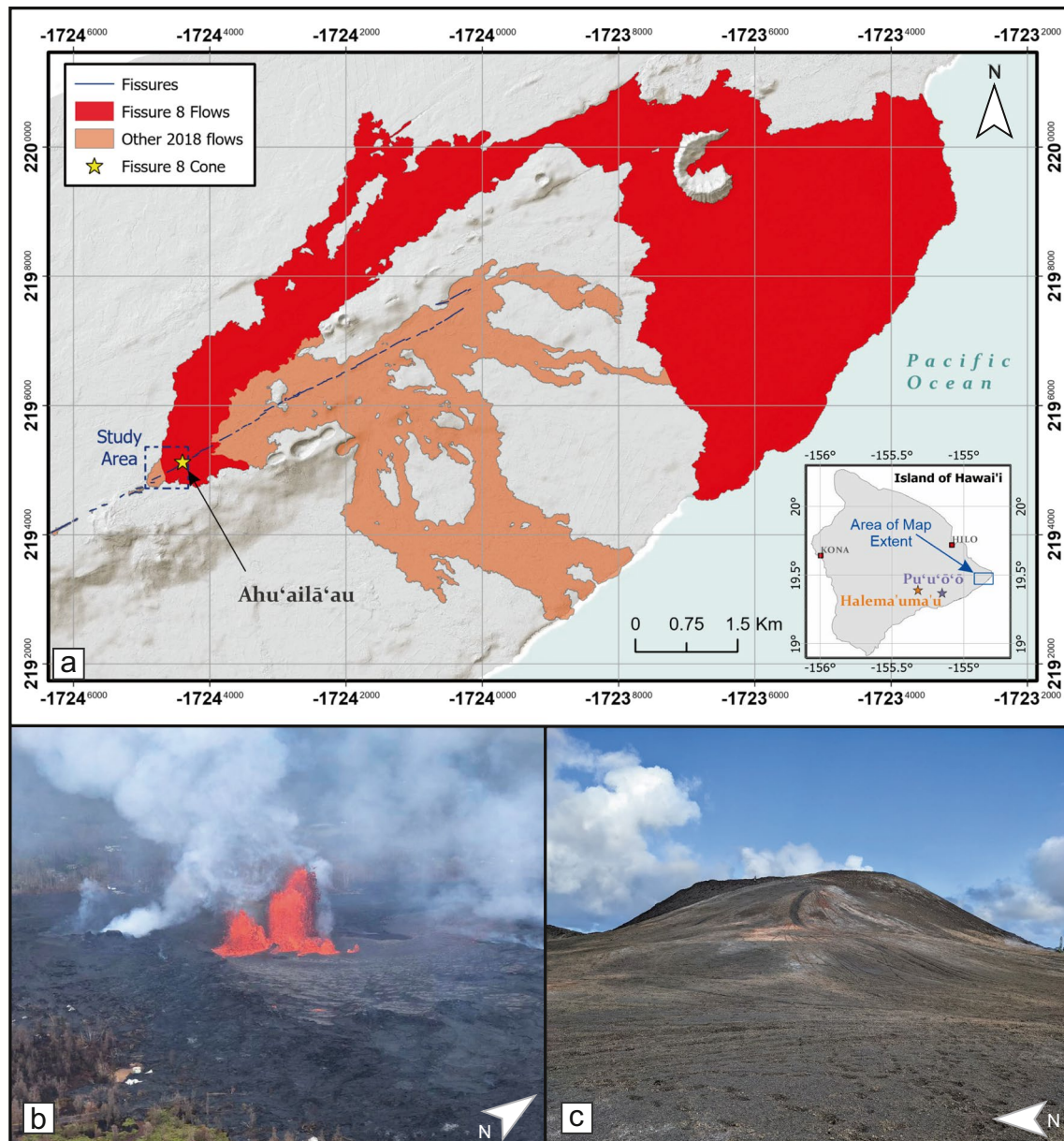2   Department of Earth Sciences, University of Hawaiʻi at Mānoa, Honolulu, HI, USA

Fig. 1 a Lava flows from the 2018 lower East Rift Zone eruption. The red flow is the main flow from fissure 8, and the orange are all other flows associated with the 2018 eruption. The star shows the location of the Ahuʻailāʻau cone. The fissures are shown as blue lines and the area of this study is outlined by the dotted box. GIS data was accessed through the USGS science data catalog: Fissure locations and lava flow areas (Zoeller et al. 2020) Lidar Digital Elevation Model (Mosbrucker et al. 2020). WGS84 UTM Zone 5N projected coordinate system used. **b** Hawaiian fountaining occurring at fissure 8 on 28 May 2018. This was early in the re-activation of fissure 8. Fountain height was approx. 60 m. Aerial photo sourced from USGS (2018). **c** Ahuʻailāʻau cone (middle distance) and tephra blanket (foreground) in 2022. Cone is approx.. 40 m tall

the compilation of isopach maps (as described by Klawonn et al. 2014a, b and Klawonn et al. 2014b), the toolboxes in-built error analysis, using Monte Carlo simulations, provide a 5 and 95% confidence interval on the volume estimations.

Whilst the number of tephra studies has increased sharply over the last few decades, only a handful of studies have investigated the tephra dispersal associated with Hawaiian fountaining events (e.g. Andronico et al. 2008; Klawonn et al. 2014a, 2014b; Mueller et al. 2018) and even fewer include a TGSD. Several reasons might account for this gap: (a) Hawaiian fountaining products often having a small dispersal area (a few square kilometres; Parfitt and Wilson 1999). This then requires scientists to enter dangerous or inaccessible proximal localities in order to obtain a collection of representative samples. Alongside this, many Hawaiian fountains are unsteady, with episodes of varied intensity,

adding an extra level of difficulty when reconstructing often necessitating episodes of contrasting intensity and dispersal within an eruption being grouped together (Klawonn et al. 2014a, 2014b); (b) even soon after an eruption, deposits are generally poorly exposed (Mueller et al. 2019) and/or eroded by wind or human activity.

Within this study, we present isopach and isopleth maps alongside a TGSD analysis of the medial tephra deposit of the main, powerful phase of the fissure 8 LERZ eruption, illustrating how aerodynamics can add complexity to the inferred eruption dynamics. The opportunity to study such a fresh deposit and subsequently continually assess its characteristics in the future will provide insight into the preservation of Hawaiian fountaining deposits. This step forward in our understanding will be of great use to the community when studying older Hawaiian fountaining eruptions.

Hawaiian fountaining

Hawaiian eruption alongside Strombolian eruptions are the most common, yet weakest, explosive volcanic eruptions to occur globally (Houghton et al. 2016). Lava fountaining can be grouped, based on height, with fountains > 400 m considered high, 100–400 moderate, and any fountain < 100 m considered low fountaining (Houghton et al. 2016). The vast majority of lava fountain eruptions at Kīlauea and worldwide are low (Houghton et al. 2016; Edwards et al. 2020) yet the associated lavas can be highly destructive. The main phase from fissure 8 during the 2018 LERZ eruption was exceptionally long-lived, lasting 93 days (Neal et al., 2019) and accounting for ~ 92–96% of the approximately 1 km^3 of erupted lava (Gansecki et al 2019). The maximum fountain height was only ~ 80 m (Lyons et al. 2021). Whilst heights provide insight into the pyroclast exit velocities and the volatile content, they do not constrain the erupted mass as this is dependent on numerous other variables including the duration of eruption and geometry of the erupting vent. The highest recorded fountaining event, Episode 16 of the 1959 Kīlauea Iki eruption, produced around 10^{10} kg of magma over a 3-h period (Richter et al. 1970), but other eruptions with low fountaining have lasted for a significantly longer duration and hence produced similar or larger erupted masses. Typically Hawaiian fountaining events have durations on the order of 10^3–10^6 s (~ 16 min to ~ 12 days) with some events, e.g. Kīlauea between 1983 and 1986, lasting for ~ 10^7 s (~ 120 days). The main F8 episode in 2018 at the LERZ was on the high end of the temporal range lasting for 93 days (Neal et al. 2019).

Products of Hawaiian fountains are mostly basaltic in composition and are initially formed by primary fragmentation by stretching and inertia of fluid magma (Gonnermann 2015). Namiki and Manga (2008) suggest that the viscosity must be < 10^6 Pa s for fragmentation to occur via this method. When the magma is erupted during fountaining, the initially molten pyroclasts cool by heat exchange with the surrounding gas and air. If the pyroclasts cool below the glass transition, they land as solid particles known as either scoria or golden pumice (lower and higher vesicularity respectively). If the time in the air is too short for the majority of a clast to cool past the glass transition, it will land as a molten fragment known as spatter. Low fountaining events or pyroclasts deposited close to the vent therefore have a lower and shorter flight and hence cooling time and often produce welded spatter deposits. A range of processes superimpose secondary fragmentation (i.e. fragmentation of pre-existing pyroclasts) on basaltic explosive eruptions, thus reducing the grain size of the final deposit. These include ductile failure of clasts falling from a lava fountain (Walker and Houghton 2019), breakup during particle–particle collisions in fountains or jets (Taddeucci et al. 2017), renewed vesiculation and brittle fragmentation of bombs (Namiki et al. 2021), and impact on landing (Richter et al. 1970).

Lower East Rift Zone 2018 eruption

Eruptive activity of Kīlauea in early 2018 was concentrated at two locations up until the onset of the LERZ eruption in May: a lava lake at the summit in Halema 'uma 'u crater, active since 2008 (Patrick et al., 2019); and Pu'u'ō'ō in the middle East Rift Zone (MERZ) with activity lasting for 35 years (Patrick et al. 2020a). The shift to the LERZ in 2018 (Fig. 1a), which resulted in the loss of over 700 buildings to lava (Patrick et al. 2020b; Neal et al. 2019), marked a change in a long settled pattern of activity at Kīlauea.

A small short-lived fissure eruption at Pu'u'ō'ō, on the middle East Rift Zone (Fig. 1), on 30 April 2018 (Neal et al. 2019), was followed by earthquakes migrating eastward into the LERZ. This seismicity, marking the eastward migration of a shallow dike system, continued throughout the next 4 days, until the LERZ eruption began when magma reached the surface at 5:00 pm HST on 3 May in Leilani Estates, at the first of 24 fissures. On 4 May 2018, a M_w 6.9 earthquake at a depth of 6 km (Neal et al. 2019) occurred on Kīlauea's south flank.

Gansecki et al. (2019) described the three main phases of the eruption. During phase 1 (3–18 May), fissures 1–20 opened (Fig. 1a). These fissures were small and short-lived, opening in a semi-random distribution. Phase 2 (17–27 May) included the opening of fissures 21–24, alongside the continued Hawaiian fountaining at other eruptive fissures, producing lava flows to the southeast. Phase 3 (28 May–4 August) saw activity focus at fissure 8 producing a scoria cone, which, in 2021, was named Ahu'ailā'au (Fig. 1; Hurley 2021; Deitterich et al., 2021). An increase of mass eruption rate during this phase resulted in a large damaging channelized lava flow travelling more than 13 km to the eastern coastline and covering an area of ~ 22

km^2 (Fig. 1; Dietterich et al. 2021). Surface discharge of magma ended on 4 August and the eruption was officially declared over on 5 September 2018. More than 1 km^3 of lava was erupted over the course of the eruption (Fig. 1; Neal et al. 2019); ~92–96% of that was erupted from fissure 8 (Gansecki et al. 2019; Fig. 1a).

During phase 3, fissure 8 underwent an intensive and prolonged period of low Hawaiian fountaining (~80 m, Lyons et al. 2021) which formed the ~40 m high scoria cone (Fig. 1). In the first week of the episode, very-low-density clasts escaped the fountain and were carried more than 600 m downwind of the vent. This focused, intensive episode coincided with the arrival of hotter, more primitive magma from the MERZ (1145°C, Gansecki et al. 2019). The high magma discharge rate in late May constructed the tephra blanket and the lower portions of Ahuʻailāʻau cone (Fig. 1), where a lava pond rapidly formed from the collapsing fountaining. In June and July, fountaining jets played to a significantly lower heights with pulsating behaviour being observed both in the jets and in the adjacent fissure 8 lava flow (Patrick et al. 2018, 2019). The detailed physical and geophysical observations, the sustained and high mass eruption rate and the highly destructive nature of the 2018 LERZ lava, makes the Ahuʻailāʻau deposits an extremely important study site for understanding the 2018 Hawaiian fountaining within the LERZ.

Methodology

Tephra thickness measurements (to the nearest cm) were carried out across the area of the continuous widespread fall deposit in February–March 2022, with all samples being obtained from within 650 m of the fissure 8 vent. The most proximal site was within 120 m of the eruptive vent. No bedding was present at the sample locations and hence no subunits have been defined.

Representative samples were collected, at 57 localities spread evenly across the study area (Figs. 4, 6), one at every location, in order to reconstruct TGSD analysis of the tephra blanket. Grain size samples were sieved down to −3.2 Φ (in 10-mm intervals, see Supplementary Material S.2) in the field with the sieved fractions and the finer grained residue weighed with a field balance. A split of the residue (tephra > −3.2 Φ, < 9.5 mm) was transported to the University of Hawaii at Manoa, and dried in a furnace at 110 °C for a minimum of 24 h. Samples were weighed pre- and post-drying to correct for moisture. The calculated moisture correction factor was then also applied to the mass of the corresponding coarser fractions of the sample sieved in the field. The dried samples then underwent further sieving, in 0.5 Φ steps down to +2.0 Φ. Everything less than +2.0 Φ accounted for less than < 3.5% for all except four samples

and so was combined in one bin (> +2.0 Φ). The four finer samples were sieved further down to +2.5 Φ where the remainder > +2.5 Φ then accounted for less than 3.5% of the total mass.

Independently at each site, we collected the largest five clasts within 5 m of the grain size and measured (to the nearest mm) the longest, shortest, and intermediate axes for each clast and averaged. Number of sample sites were limited compared to other comparable studies (e.g. Mueller et al. 2018), however quantitatively still within acceptable limits as investigated by Klawonn et al. (2014a and 2014b).

Density and bulk vesicularity analyses were carried out on two suites of 16–32-mm clasts (following Houghton and Wilson 1989): 200 clasts from two sites combined and presented together as the F8 medial deposit (F8d; 19.44985°N 154.91415°W and 19.45579°N 154.91771°W), and 167 clasts representative of the Ahuʻailāʻau cone (F8c; 19.461071°N 154.909198°W). Density measurements were made following Houghton and Wilson (1989), and vesicularities calculated using a dense rock equivalent of 2800 kg m^{-3}.

Isopach maps of the widespread tephra blanket deposit were drawn by hand, with the most distal isopach being 10 cm. Thickness of deposits beyond this contour could not be constrained with confidence in the field due to reworking of the deposit through wind, weather, and human interference. The isopach areas were then calculated through Arc-GIS Pro. Deposit thinning and volume calculations were constrained using the TephraFits model (Biass et al. 2019b) which applies three empirical thinning relationships (Exponential, Power-Law and Weibull) to the available data. We specified a 7% uncertainty on the isopach areas when using the TephraFits model as this was approximated for a well-sampled medial deposit within Klawonn et al. (2014b). Overall uncertainty in the model fitting (using a 5 and 95% confidence interval calculated using an inbuilt Monte-Carlo approach) results in volume estimate errors of approximately ± 12% (Table 1).

Total grain size distribution of the widespread fall (i.e. excluding tephra forming the cone or incorporated into the lava flow) was estimated using the Voronoi tessellation

Table 1 Volume estimates of the Fissure 8 tephra blanket deposit using three empirical thinning relationships: exponential (Fierstein and Nathenson 1992), power-law (Bonadonna and Houghton; 2005), and Weibull (Bonadonna and Costa 2012; 2013). Values calculated using TephraFits model (Biass et al. 2019a, b)

	Volume (m^3)	R^2	Volume min (m^3)	Volume max (m^3)
Exponential	1.57×10^4	0.989	1.40×10^4	1.76×10^4
Power-law	1.99×10^4	0.994	1.82×10^4	2.22×10^4
Weibull	2.13×10^4	0.991	1.95×10^4	2.36×10^4

method (Bonadonna and Houghton 2005). Voronoi tessellation creates cells around every sample location, with each edge being a bisector of the line segment that would connect that sample location to a surrounding sample. This method ensures that the cell only includes grid points which are closer to those samples than any other. Once the cells have been created, each cell is assigned the deposit thickness, mass loading (calculated using a bulk density of 0.2 kg m^{-3}), and grain size distribution (GSD) of the corresponding sample. The TGSD is obtained from the mass-loading and area-weighted average of all the cells within the deposit. The Voronoi TGSD results presented here were calculated using the MATLAB code TOTGS (Biass and Bonadonna 2014). The code requires a zero-isopach-contour, which was estimated based on extrapolation of the deposit; however, the calculation is not sensitive to the positioning of the zero-isopach-contour at the scale of the deposit within this study.

For each grain size dataset associated with a sampling site, a cumulative frequency line was drawn based on the raw data obtained through the sieving (see Supplementary Material S.2). Regular interval grain size values, the Inman coefficient ([Φ_{84}–Φ_{16}]/2), and median diameter (Φ_{50}; Fig. 9) have been calculated by extracting the associated phi values (e.g. Φ_{16}, Φ_{50}, Φ_{84}) from the cumulative frequency curves for each individual sample (Fig. 7a). The modal grain size for each sample was assessed by looking at the phi values over which the cumulative frequency line had the greatest gradient.

Results

General characteristics of the ejecta

The proximal products of the F8 fountain constitute the scoria cone of Ahu'ailā'au (Fig. 1), which is dominated by large (i.e. > 64 mm) fluidal clasts (Fig. 2), with minor Pele's hair and tears, with fluidal textures being very common on all large clasts forming the surface of the cone, indicating the core of the bombs had not completely crossed the glass-transition, allowing them to continue to vesiculate, deform,

and sometimes weld and/or flow after landing. However, this is not true about all the pyroclasts on the cone: some (scoria) landed in a solid state. A large range in vesicularity (36 to 95 volume %) was observed on the scoria cone, similar to that previously reported (i.e. 41 to 96 volume %; Namiki et al. 2021). Namiki et al. (2021) proposed that the high vesicularities result from secondary vesiculation, as a consequence of rapid bubble nucleation and adiabatic gas expansion, subsequently causing further (i.e. secondary) fragmentation.

The widespread medial tephra blanket deposit is lapilli-dominated with a large proportion of reticulite and minor golden pumice (Fig. 2). Negligible abundances of larger fluidal clasts (Fig. 2) and Pele's tears and hair were also observed. Widely separated, decimetre-diameter, highly vesicular bombs were commonly observed but were often broken either from the impact upon landing, or from human influence post-eruption. Distal tephra, which formed a fringe surrounding the preserved medial fall, were, at the time of our mapping, very poorly preserved and have mostly been reworked or removed by residents during clean-up operations.

Vesicularity

The effect of the secondary fragmentation at the top of the highest F8 fountains, described by Namiki et al. (2021), is not only a significant reduction in clast size but also a major change in vesicularity and hence density of the clast population. The medial deposit is dominated by reticulite clasts (Fig. 2) with density 100–300 kgm^{-3} (Fig. 3), containing 91 to 97 volume % of c. 1-mm vesicles of very uniform size. A smaller subpopulation of clasts contains small vesicles together with scattered mm-cm bubbles (golden pumice, 82 to 91% vesicles, Fig. 2). Clasts from the cone are dominantly black scoria (Fig. 2) with a broad range of vesicularity from 42 to 79% vesicularity and density of 500–1750 kgm^{-3} (Fig. 3). Cone-forming clasts reflect only the primary magmatic fragmentation at the base of the fountain. Namiki et al. (2021) suggest that, in the medial deposit, the signature of primary fragmentation has been overprinted by a short but intense period of bubble nucleation accompanying secondary fragmentation at the top of the fountain.
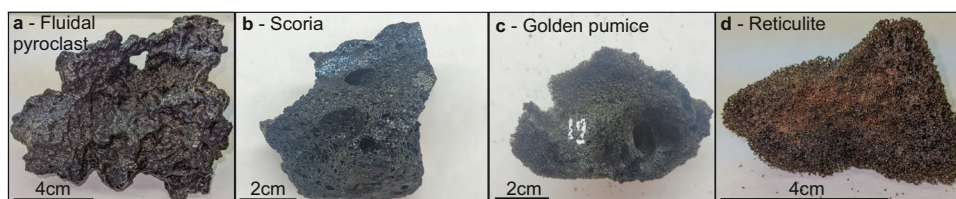

Fig. 2 Photos of typical pyroclasts obtained from the cone-forming (**a**, **b**) and medial (**c**, **d**) F8 tephra deposit. **a** Fluidal pyroclast ~ 10 cm in size. **b** Scoria ~ 6 cm in size. **c** Golden pumice ~ 7 cm in size, **d** reticulite ~ 6 cm in size
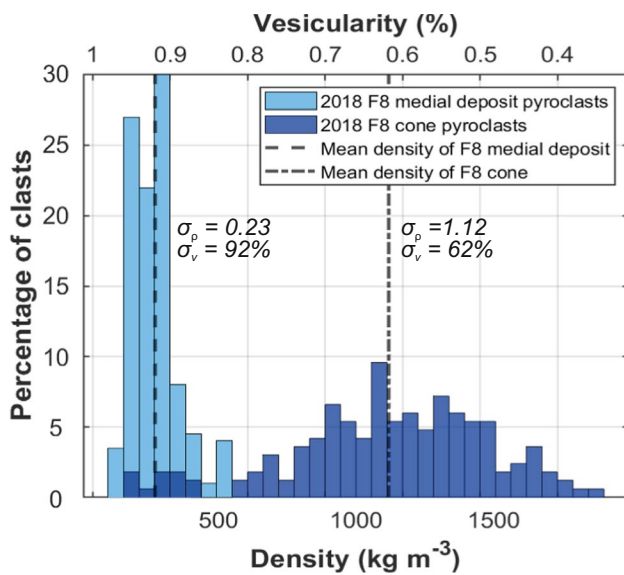
Fig. 3 Distribution of density within the pyroclasts from the medial deposit (light blue) and the Ahuʻailāʻau cone (dark blue). Mean for each deposit is shown by the dashed and dot-dashed lines respectively
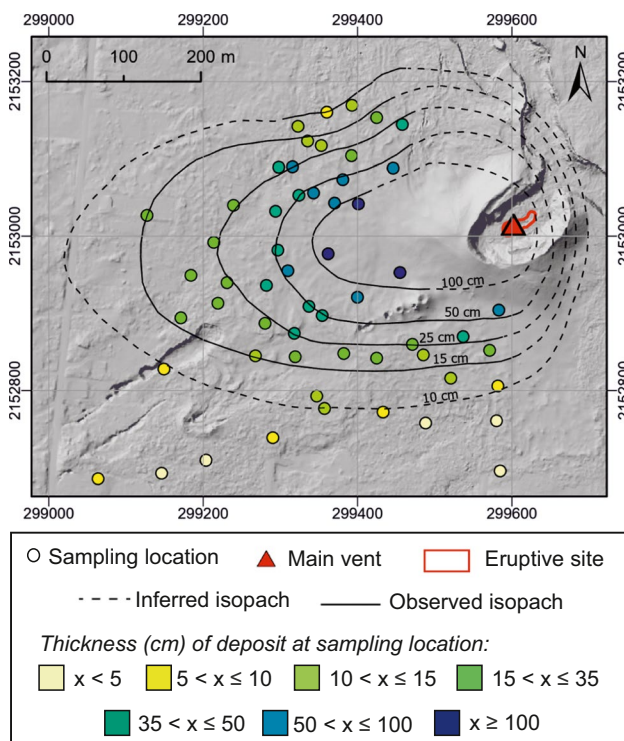

Fig. 4 Isopach map of the tephra blanket formed during the eruption sourced fissure 8. Contour thicknesses are 10 cm, 15 cm, 25 cm, 50 cm, and 100 cm. Sampling locations are shown by the dots with the colour corresponding to the measured thickness of the deposit. The red triangle shows the location of the principal eruptive vent. DEM is from Mosbrucker et al. (2020). Coordinate system as for Fig. 1

Thickness and isopach map

The dispersal axis is 265° which aligns with the observed dominant easterly wind direction in Leilani Estates in May 2018. The thinning of the tephra blanket is approximately exponential. The thickness of the deposit decreases by a factor of two approximately every 60 m when on-axis and within 300 m of the vent. The most distal deposits have a thinning distance of approximately 90 m, where the deposit is about 10 cm thick.

The isopach map (Fig. 4) of the tephra blanket is based on field thickness data collected by the authors (see Supplementary Material S.2). Thickness considerations meant that Ahuʻailāʻau cone and the ejecta that formed the rheomorphic lava flow were not included in the isopach map or volume estimates. The closest data point was ~ 120 m from the erupting vent (Fig. 3). Five isopach contours have been closed (Fig. 4), with the smallest isopach (10 cm) covering an area of 0.22 ± 0.009 km^2. This was the smallest isopach recorded due to the poor preservation of the thin deposits falling in the adjacent residential environments. The four other isopach contours are very well constrained (Fig. 4; Supplementary Material S.1) with the areas of each shown in Supplementary Material S.2. A few thickness measurements were not included in the isopach map as they appeared to be anomalies. These anomalies can be explained due to two reasons: (1) proximity to cleared access roads and thus likely to have been affected by human interference; (2) shadow effects (i.e. atmospheric turbulence) as a result of some subsidiary cones (Fig. 6).

Volume estimates

Volume estimates of the tephra blanket (not including Ahuʻailāʻau and the lava flow) have been calculated based on the isopach areas using the TephraFits model (Biass et al. 2019b) and are shown in Table 1 and Fig. 5. The TephraFits model applied three empirical thinning relationships (exponential, power-law and Weibull) to the isopach contour areas.

All three relationships offer excellent fits to the data ($R^2 = 0.99$) despite the lack of distal data. The lack of distal constraints was a result of the modification of the deposit by wind/weather erosion and most commonly human interference due to the deposit falling on a housing estate. The total volume of the medial deposit is estimated to be $1.57 \times 10^4 \pm 0.19$ m^3 (exponential), $2.13 \times 10^4 \pm 0.22$ m^3 (Weibull), and the best fit thinning relationship (power-law) returned a volume of $1.99 \times 10^4 \pm 0.23$ m^3 (Fig. 5b). This is just 0.02% of the total volume erupted from the main episode of F8 in 2018 (Neal et al. 2019); the remainder is contained within the proximal cone and the rheomorphic lava flow.
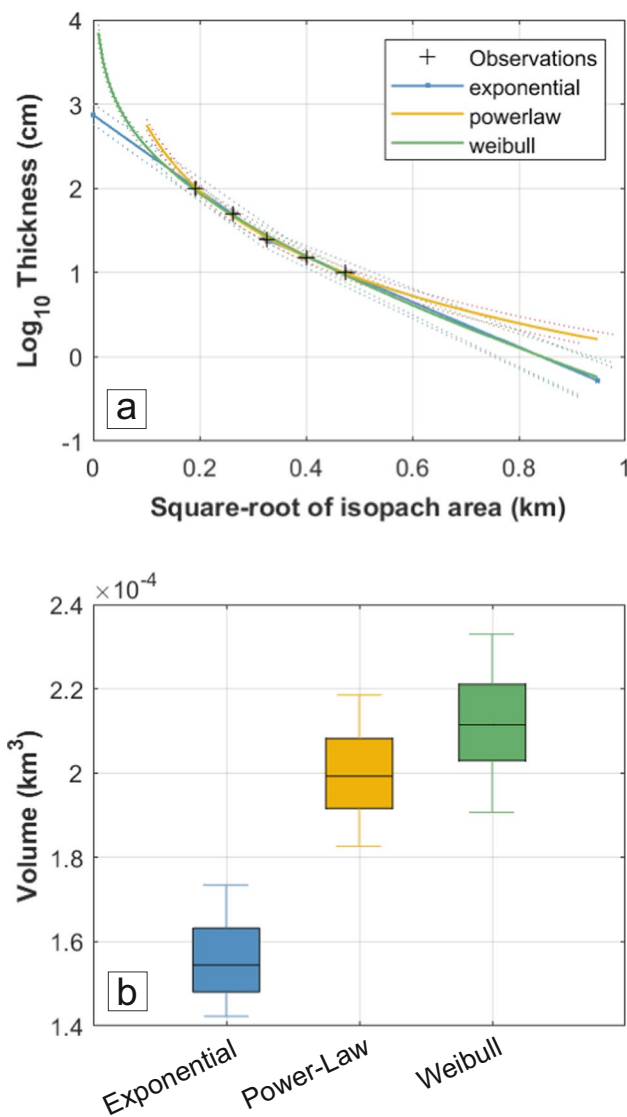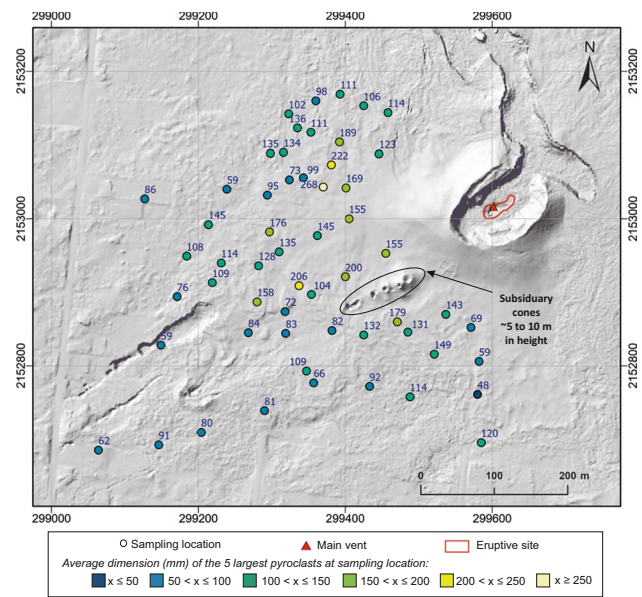
Fig. 6 Map showing the sampling locations (circles) and the average size (mm) of the 5 largest clasts within 5 m of each sample location (shown by the corresponding fill colour). No contours (isopleth lines) have been plotted due to lack of spatial patterns observed. Principal eruptive vent is shown by the red triangle and the DEM is from Mosbrucker et al. (2020). Note the five small subsidiary vents to the southwest of the main cone (approximately 5 to 10 m in height). Coordinate system as in Fig. 1

Fig. 5 **a** Log thickness vs square root of area plot showing the thinning of the deposit. Crosses represent the actual observed thickness points and the three fits, i.e. exponential, power-law, and Weibull are displayed by blue, yellow and green lines respectively. The 5 h and 95th percentile confidence interval are shown by dotted lines in the corresponding colour. **b** Box and whisker plots for volume estimates of each of the empirical thinning laws. Colours correspond to the style of fit as in **a**. The box shows the 1st and 3rd quartiles. The ends of the whiskers show the 5th and 95th percentile

were often broken; as a result, they were never observed deeper in the deposit. When mapping the sizes of the largest clasts across the study area, the distribution does not show a clear pattern and hence no isopleth lines have been plotted (Fig. 6).

Grain size distribution (GSD) of single samples is consistent across the whole study area showing minimal fining with distance from the vent (Fig. 7a). Lapilli ($-5.5 < \Phi < -1$) dominated the GSD contributing 80.9–96.3 wt% to the deposit volume in all samples. The mode of all the measured samples was within the range of -4 to $-3.5\ \Phi$ with 60% of the samples having a modal grain size of $-3.5\ \Phi$ and the remaining 40% having a mode grain size of $-4\ \Phi$. The amount of tephra estimated from the Voronoi tessellation TGSD (cells shown in Fig. 7c) was 91.8 wt% lapilli and the mode was $-3.5\ \Phi$. A few anomalously coarse grain size distributions can be observed both close to (160–170 m) and farther from vent (>500 m). The anomalously coarse samples away from the vent are frequently in locations that have been obstructed by the minor scoria cones southeast of Ahuʻailāʻau indicating complex aerodynamics and re-entrainment of large clasts close to the ground, occurred, disrupting the typical tephra settling pattern. Rare finer samples can also be observed (Fig. 7a), which may reflect (1) contamination by late-stage ash through re-dispersal by the wind or (2) human activity, crushing clasts producing a high proportion of fine tephra.

Grain size distribution

All samples (57 sample locations) contain lapilli ($-6 < \Phi < -1$) and ash ($\Phi > -1$) with the finest ash being 2.5 Φ (0.2 mm). Particles finer than 1.5 Φ make up a maximum of 3.5 wt% of the samples. The grain size range of the analysed samples is -6 to 2.5 Φ (64–0.2 mm). Bombs ranging in size from -8.6 to -6 Φ (410 to 64 mm) could be found on the surface of the tephra deposit at (within 5-m radius) every sample location. The bombs

Fig. 7 **a** Cumulative frequency plot, showing the grain size distribution of 55 samples colour-coded with distance from the vent. Yellow being medial and blue being close to vent. Black dashed line shows the results from Voronoi TGSD (labelled TOTGS). **b** Values of the 16th (yellow circles), 50th (green diamonds), and 84th (blue squares) percentiles for all 55 samples illustrating how the percentiles used as statistic parameters for sorting vary with distance from the eruptive vent. **c** Map showing the Voronoi cells, applied to the tephra blanket of F8, used to calculate the TGSD. Each cell represents a Voronoi cell built around each sample point (blue dots). The outermost line represents the estimated line of zero mass
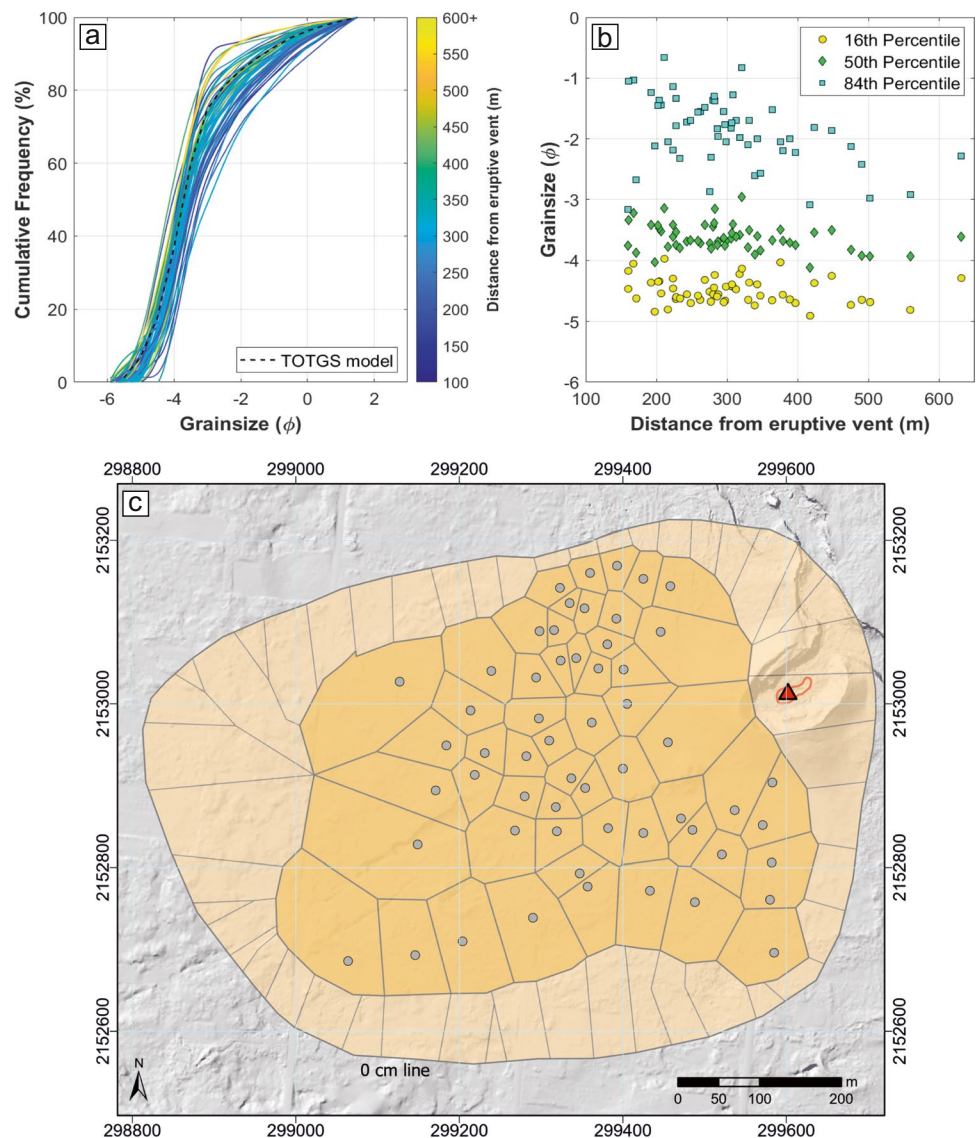
Discussion

Tephra production and re-entrainment

The anomalous thickness measurements (see the "Thickness and isopach map" section) and sample sizes (see the "Grain size distribution" section) at fissure 8 could be explained through two main reasons: (1) the four/five subsidiary cones to the southwest (Fig. 6) created a shadow zone in which near surface wind gusts formed an local atmospheric circulation system, which re-entrained large clasts that were carried beyond the subsidiary cones (Fig. 8). Re-entrainment would have been facilitated by a secondary vesiculation event as described by Namiki et al. (2021). Secondary vesiculation produced the dominant population reticulite/golden pumice clasts with extremely low density, which in turn enabled their re-lifting by upwelling air parcels (i.e. local

atmospheric circulatory systems), much like the movement of a feather (Fig. 8). (2) The duration of time since the tephra has been deposited opened up the possibility of fragmentation and degradation of the deposit through human activity (i.e. people walking over the deposit, and clearing tephra off their land). We propose that it was a combination of these mechanisms that resulted in the high modal grain size and anomalously coarse particles of the deposit observed today.

It should be noted that whilst it had only been 4 years since the F8 eruption when carrying out the field campaigns, human interference (i.e. clearing the deposit from properties/roads and walking/driving over deposit) was evident. In this study, it was clear where this had occurred and hence these areas were avoided, thereby minimising the impact of these interferences on the calculations in this study. This human interaction likely increases over time as people regain the land, and therefore, in future studies
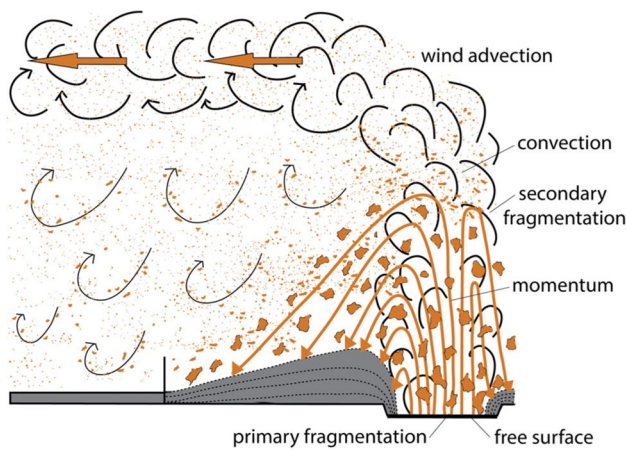
Fig. 8 Schematic overview of the Fissure 8 vent Hawaiian fountaining up to 80 m high. Secondary vesiculation within the ejecta results in further fragmentation (referred to as secondary fragmentation). The ejecta can be seen to be dispersed with the low-density pyroclasts (reticulite/golden pumice) being re-entrained by the local upwelling air parcels resulting in an unusual distribution of medial clasts. Adapted from Mueller et al. (2018)

the inhabitancy levels and duration of time since eruption should be strongly considered when assessing the potential errors on field measurements.

Comparisons with other lava-fountaining eruptions

There are no well-studied medial deposits of other lava-fountaining eruptions that match the grain size characteristics of the F8 deposits closely. In general, the 20 well-studied deposits collated by Costa et al. (2016) are for other more powerful eruption styles and are typified by two overlapping grain size populations. This bimodality is inferred to reflect contrasting transport modes but not necessarily different fragmentation histories, as inferred by Namiki et al. (2021) for the F8 deposits. Of the 20 deposits used by Costa et al. (2016), only one (Etna 2007) is of moderate Hawaiian intensity (Fig. 9).

The most intensively sampled Hawaiian medial fall is that of Kīlauea Iki in 1959 (Richter et al. 1970; Klawonn et al. 2014a, 2014b; Mueller et al. 2018). The mode of its TGSD is −2 phi, one phi unit finer than the F8 medial deposit. This is predictable given that the 1959 fall was the product of generally higher lava fountaining and was constrained out to 4 km from vent (Mueller et al. 2019). The widespread deposit mostly contains a mixture of golden pumice and fluidal clasts, with wider ranges of vesicle sizes than present in reticulite, which was interpreted as the products of a single primary vesiculation event over a prolonged time interval extending past the time of fragmentation (Stovall et al. 2011; 2012). A much smaller amount of true reticulite was erupted (Richter et al. 1970) but mostly blown by the strong
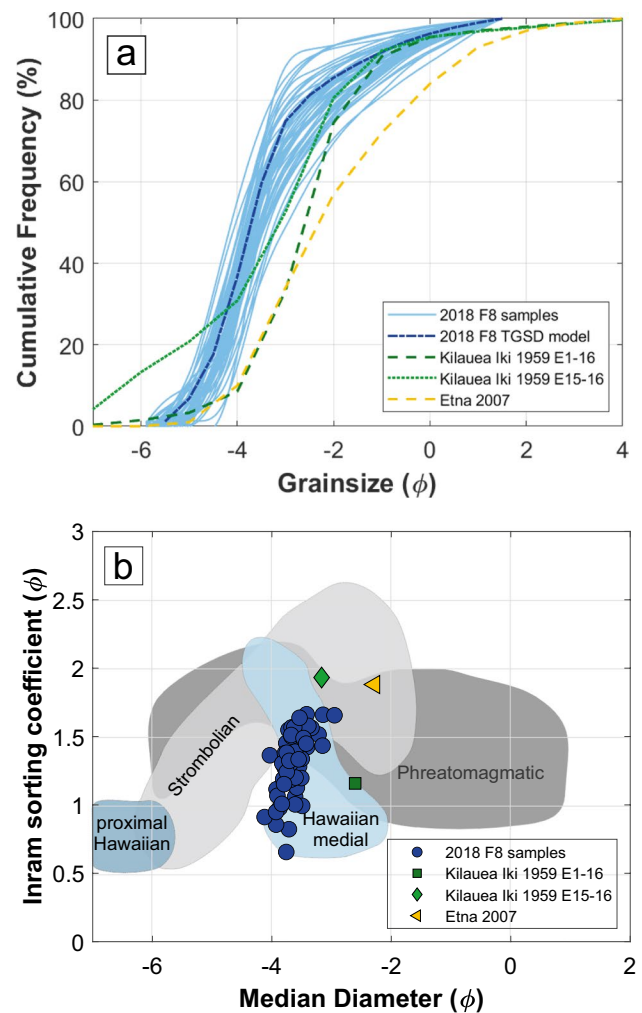

Fig. 9 Inman sorting coefficient (Φ_{84}–Φ_{16})/2 against median diameter (Φ_{50}) illustrating the grain size characteristics of the tephra blanket (blue circles, see the "Methods" section for details on calculation). Reference fields of deposits from medial Hawaiian fountaining (light blue), Strombolian activity (light grey), and Phreatomagmatic activity (dark grey) are shown (after Sigurdsson et al. 2015). Hawaiian proximal field (dark blue) is after Houghton et al. (2021). The average of Kīlauea Iki deposits (green) and Etna 2007 deposits (yellow) are displayed for comparison

winds beyond the limits of the continuous tephra sheet. At the peaks of the highest fountaining episodes (3, 15, 16), dense scoria clasts were also transported beyond the 1959 cone, to distances up to 500 m from the vent.

In general, the more powerful deposits that Costa et al. (2016) collated are typified by two overlapping grain size populations inferred to reflect contrasting ballistic and convective transport. Ballistic clasts do not extend into the medial 2018 LERZ products, and the distinction between the our data and that from the other lava-fountaining eruptions cited by Costa et al. is a function of our inability to sample the coarse-grained, but intensely welded 2018 cone.

Conclusions

Very high clast vesicularities during the final phase of lava fountaining from F8 in 2018 led to distribution of the pyroclasts as a widespread fall beyond the proximal scoria cone. This subpopulation of exceptionally light pyroclasts was able to escape from the top of the fountain with the decoupled gas phase whilst the numerically dominant denser clasts fell from the fountain to form the cone and fed the associated lava flow. The very light reticulite/golden pumice clasts were strongly affected by fluctuations and eddies in the near surface wind field, being re-entrained into plumes especially in the lee of subsidiary vents to the southwest of the cone (Fig. 8). The lack of a systematic fall-off in maximum clasts size with distance from vent which is typical for pyroclastic fall deposits (Sigurdsson et al. 2015) can be explained by this re-entrainment process.

References

Andronico D, Cristaldi A, Scollo S (2008) The 4–5 September 2007 lava fountain at South-East Crater of Mt Etna, Italy. J Volcanol Geoth Res 173(3–4):325–328. https://doi.org/10.1016/j.jvolgeores.2008.02.004

Biass S, Bonadonna C (2014) TOTGS: Total grainsize distribution of tephra fallout. https://doi.org/10.5281/zenodo.3590597

Biass S, Bonadonna C, Houghton BF (2019a) A step-by-step evaluation of empirical methods to quantify eruption source parameters from tephra-fall deposits. J Appl Volcanol 8:1–16. https://doi.org/10.1186/s13617-018-0081-1

Biass S, Bonadonna C, Houghton BF (2019b) TephraFits. https://doi.org/10.5281/zenodo.3590642

Bonadonna C, Costa A (2012) Estimating the volume of tephra deposits: a new simple strategy. Geology 40(5):415–418. https://doi.org/10.1130/G32769.1

Bonadonna C, Costa A (2013) Plume height, volume, and classification of explosive volcanic eruptions based on the Weibull function. Bull Volcanol 75(8):1–19. https://doi.org/10.1007/s00445-013-0742-1

Bonadonna C, Houghton BF (2005) Total grain-size distribution and volume of tephra-fall deposits. Bull Volcanol 67(5):441–456. https://doi.org/10.1007/s00445-004-0386-2

Costa A, Pioli L, Bonadonna C (2016) Assessing tephra total grain-size distribution: Insights from field data analysis. Earth Planet Sci Lett 443:90–107. https://doi.org/10.1016/j.epsl.2016.02.040

Dietterich HR, Diefenbach AK, Soule SA, Zoeller MH, Patrick MP, Major JJ, Lundgren PR (2021) Lava effusion rate evolution and erupted volume during the 2018 Kīlauea lower East Rift Zone eruption. Bull Volcanol 83(4):1–18. https://doi.org/10.1007/s00445-021-01443-6

Edwards MJ, Pioli L, Harris AJ, Gurioli L, Thivet S (2020) Magma fragmentation and particle size distributions in low intensity mafic explosions: the July/August 2015 Piton de la Fournaise eruption. Sci Rep 10(1):1–14. https://doi.org/10.1038/s41598-020-69976-y

Fierstein J, Nathenson M (1992) Another look at the calculation of fallout tephra volumes. Bull Volcanol 54(2):156–167. https://doi.org/10.1007/BF00278005

Gansecki C, Lee RL, Shea T, Lundblad SP, Hon Parcheta C. (2019). The tangled tale of Kīlauea's 2018 eruption as told by geochemical monitoring. *Science*, 366(6470). https://doi.org/10.1126/science.aaz0147

Gonnermann HM (2015) Magma fragmentation. Annu Rev Earth Planet Sci 43:431–458. https://doi.org/10.1146/annurev-earth-060614-105206

Horwell CJ, Michnowicz SAK, Le Blond JS (2008) Report on the mineralogical and geochemical characterisation of Hawai'i ash for the assessment of respiratory health hazard. *International volcanic health hazard network*. https://www.ivhhn.org/uploads/IVHHN_Hawaii_report_2008.pdf. Accessed 12 Feb 2023

Houghton BF, Wilson CJN (1989) A vesicularity index for pyroclastic deposits. Bull Volcanol 51:451–462. https://doi.org/10.1007/BF01078811

Houghton BF, Taddeucci J, Andronico D, Gonnermann HM, Pistolesi M, Patrick MR, Orr TR, Swanson DA, Edmonds M, Gaudin D, Carey RJ (2016) Stronger or longer: discriminating between Hawaiian and Strombolian eruption styles. Geology 44(2):163–166. https://doi.org/10.1130/G37423.1

Houghton BF, Tisdale CM, Llewellin EW, Taddeucci J, Orr TR, Walker BH, Patrick MR (2021) The birth of a Hawaiian fissure eruption. J Geophysical Res: Solid Earth 126(1):e2020JB020903

Sigurdsson H, McNutt S, Rymer H, Stix J (2015) The encyclopedia of volcanoes, 2nd edn. Academic Press

Hurley T (2021) Kilauea's fissure 8 gets a name. https://www.staradvertiser.com/2021/03/04/breaking-news/kilaueas-fissure-8-gets-a-name/. Accessed 21 April 2022.

Jenkins SF, McGill CR, Blong RJ (2018) Evaluating relative tephra fall hazard and risk in the Asia-Pacific region. Geosphere 14:492–509. https://doi.org/10.1130/GES01549.1

Jenkins SF, Wilson TM, Magill CR, Miller V, Stewart C, Blong R, Marzocchi W, Boulton M, Bonadonna C, Costa A (2015) Volcanic ash fall hazard and risk. In: Loughlin, S.C., et al., eds., Global Volcanic Hazards and Risk. Cambridge University Press, Cambridge, pp 173–222. https://doi.org/10.1017/CBO9781316276273.005

Klawonn M, Houghton BF, Swanson DA, Fagents SA, Wessel P, Wolfe CJ (2014a) Constraining explosive volcanism: subjective choices during estimates of eruption magnitude. Bull Volcanol 76(2):1–6. https://doi.org/10.1007/s00445-013-0793-3

Klawonn M, Houghton BF, Swanson DA, Fagents SA, Wessel P, Wolfe CJ (2014b) From field data to volumes: constraining uncertainties in pyroclastic eruption parameters. Bull Volcanol 76:1–16. https://doi.org/10.1007/s00445-014-0839-1

Longo BM, Yang W, Green JB, Crosby FL, Crosby VL (2010) Acute health effects associated with exposure to volcanic air pollution (vog) from increased activity at Kilauea Volcano in 2008. J Toxicol Environ Health A 73(20):1370–1381. https://doi.org/10.1080/15287394.2010.497440

Longo BM (2013) Adverse health effects associated with increased activity at Kīlauea Volcano: a repeated population-based survey. Int Scholarly Res Notices 475962. https://doi.org/10.1155/2013/475962

Lyons JJ, Dietterich HR, Patrick MP, Fee D (2021) High-speed lava flow infrasound from Kīlauea's fissure 8 and its utility in monitoring effusion rate. Bull Volcanol 83:1–12. https://doi.org/10.1007/s00445-021-01488-7

Meredith ES, Jenkins SF, Hayes JL, Deligne NI, Lallemant D, Patrick M, Neal C (2022) Damage assessment for the 2018 lower East Rift Zone lava flows of Kīlauea volcano. Hawai'i Bulletin of Volcanology 84(7):65. https://doi.org/10.1007/s00445-022-01568-2

Mosbrucker AR, Zoeller MH, Ramsey DW (2020) Digital elevation model of Kilauea Volcano, Hawaii, based on July 2019 airborne lidar surveys. https://doi.org/10.5066/P9F1ZU8O. Accessed 5 Feb 2022

Mueller SB, Houghton BF, Swanson DA, Fagents SA, Klawonn M (2018) Intricate episodic growth of a Hawaiian tephra deposit: case study of the 1959 Kīlauea Iki eruption. Bull Volcanol 80(10):1–19. https://doi.org/10.1007/s00445-018-1249-6

Mueller SB, Houghton BF, Swanson DA, Poret M, Fagents SA (2019) Total grain size distribution of an intense Hawaiian fountaining event: case study of the 1959 Kīlauea Iki eruption. Bull Volcanol 81(7):1–13. https://doi.org/10.1007/s00445-019-1304-y

Namiki A, Manga M (2008) Transition between fragmentation and permeable outgassing of low viscosity magmas. J Volcanol Geoth Res 169(1–2):48–60. https://doi.org/10.1016/j.jvolgeores.2007.07.020

Namiki A, Patrick MR, Manga M, Houghton BF (2021) Brittle fragmentation by rapid gas separation in a Hawaiian fountain. Nat Geosci 14(4):242–247. https://doi.org/10.1038/s41561-021-00709-0

Neal CA, Brantley SR, Antolik L, Babb JL, Burgess M, Calles K, Cappos M, Chang JC, Conway S, Desmither L, Dotray P (2019) The 2018 rift eruption and summit collapse of Kīlauea Volcano. Science 363(6425):367–374. https://doi.org/10.1126/science.aav7046

Parfitt EA, Wilson L (1999) A Plinian treatment of fallout from Hawaiian lava fountains. J Volcanol Geoth Res 88(1–2):67–75. https://doi.org/10.1016/S0377-0273(98)00103-6

Patrick MR, Houghton BF, Anderson KR, Poland MP, Montgomery-Brown E, Johanson I, Thelen W, Elias T (2020a) The cascading origin of the 2018 Kīlauea eruption and implications for future forecasting. Nat Commun 11(1):1–13. https://doi.org/10.1038/s41467-020-19190-1

Patrick M, Johanson I, Shea T, Waite G (2020b) The historic events at Kīlauea Volcano in 2018: summit collapse, rift zone eruption, and Mw 6.9 earthquake: preface to the special issue. Bulletin Volcanol 82(6):1–4. https://doi.org/10.1007/s00445-020-01377-5

Patrick MR, Orr TR, Swanson DA, Elias T, Shiro B (2018) Lava lake activity at the summit of Kīlauea Volcano in 2016. Geological Survey Scientific Investigations Report 2018–5008, 58 p. https://doi.org/10.3133/sir20185008

Patrick MR, Dietterich HR, Lyons JJ, Diefenbach AK, Parcheta C, Anderson KR, Namiki A, Sumita I, Shiro B, Kauahikaua JP (2019) Cyclic lava effusion during the 2018 eruption of Kīlauea Volcano. Science. 366(6470). https://doi.org/10.1126/science.aav9070

Richter DH, Eaton JP, Murata KJ, Ault WU, Krivoy HL (1970) Chronological narrative of the 1959–60 eruption of Kilauea volcano, Hawaii (No. 537-E). US Geological Survey https://doi.org/10.3133/pp537E

Stovall WK, Houghton BF, Gonnermann H, Fagents SA, Swanson DA (2011) Eruption dynamics of Hawaiian-style fountains: the case study of episode 1 of the Kīlauea Iki 1959 eruption. Bull Volcanol 73:511–529. https://doi.org/10.1007/s00445-010-0426-z

Stovall WK, Houghton BF, Hammer JE, Fagents SA, Swanson DA (2012) Vesiculation of high fountaining Hawaiian eruptions: episodes 15 and 16 of 1959 Kīlauea Iki. Bull Volcanol 74:441–455. https://doi.org/10.1007/s00445-011-0531-7

Taddeucci J, Alatorre-Ibargüengoitia MA, Cruz-Vázquez O, Del Bello E, Scarlato P, Ricci T (2017) In-flight dynamics of volcanic ballistic projectiles. Rev Geophys 55(3):675–718. https://doi.org/10.1002/2017RG000564

USGS (2018) https://www.usgs.gov/media/images/fissure-8-reactivated-afternoon-may-28-and-times-was. Accessed 20 Apr 2022

Walker BH, Houghton BF (2019) December. Secondary fragmentation of pyroclasts during Hawaiian fountaining in 2018. In AGU Fall Meeting Abstracts (2019, V13E-0213)

Wilson TM, Stewart C, Sword-Daniels V, Leonard GS, Johnston DM, Cole JW, Wardman J, Wilson G, Barnard ST (2012) Volcanic ash impacts on critical infrastructure. Physics and Chemistry of the Earth 45:5–23. https://doi.org/10.1016/j.pce.2011.06.006

Zoeller MH, Perroy RL, Wessels R, Fisher GB, Robinson JE, Bard J A, Peters J, Mosbrucker A, Parcheta CE (2020) Geospatial database of the 2018 lower East Rift Zone eruption of Kilauea Volcano, Hawaii https://doi.org/10.5066/P9S7UQKQ